

Article

All-Inorganic CsPbBr₃ Perovskite Nanocrystals Synthesized with Olive Oil and Oleylamine at Room Temperature

Getachew Welyab^{1,2}, Muluaem Abebe¹, Dhakshnamoorthy Mani¹ , Aparna Thankappan³ , Sabu Thomas⁴, Fekadu Gochole Aga^{5,6} and Jung Yong Kim^{5,6,*} 

¹ Faculty of Materials Science and Engineering, Jimma Institute of Technology, Jimma University, Jimma P.O. Box 378, Ethiopia; gwelyabt@gmail.com (G.W.); muabeme@gmail.com (M.A.); m.dhakshnamoorthy@gmail.com (D.M.)

² Department of Physics, College of Natural and Computational Science, Mizan-Tepi University, Mizan P.O. Box 260, Ethiopia

³ Department of Physics, Baselius College, Kottayam 686001, India; aparnathankappan@baselius.ac.in

⁴ School of Energy Materials, Mahatma Gandhi University, Kottayam 686560, India; sabuthomas@mgu.ac.in

⁵ Department of Materials Science and Engineering, Adama Science and Technology University, Adama P.O. Box 1888, Ethiopia; fekadu.gochole@astu.edu.et

⁶ Center of Advanced Materials Science and Engineering, Adama Science and Technology University, Adama P.O. Box 1888, Ethiopia

* Correspondence: jungyong.kim@astu.edu.et

Abstract: Room temperature (RT) synthesis of the ternary cesium lead bromide CsPbBr₃ quantum dots with oleic acid and oleylamine ligands was developed by Zeng and coworkers in 2016. In their works, the supersaturated recrystallization (SR) was adopted as a processing method without requiring inert gas and high-temperature injection. However, the oleic acid ligand for haloplumbate is known to be relatively unstable. Hence, in this work, we employed the eco-friendly olive oil to replace the oleic acid portion for the SR process at RT. Resultantly, we found that the cube-shaped nanocrystal has a size of ~40–42 nm and an optical bandgap of ~2.3 eV independent of the surface ligands, but the photoluminescence lifetime (τ_{av}) and crystal packing are dependent on the ligand species, e.g., τ_{av} = 3.228 ns (olive oil and oleylamine; here less ordered) vs. 1.167 ns (oleic acid and oleylamine). Importantly, we explain the SR mechanism from the viewpoint of the classical LaMer model combined with the solvent engineering technique in details.

Keywords: perovskite; supersaturated recrystallization; CsPbBr₃; olive oil; LaMer model; nucleation and growth; solvent engineering; nanocrystals; quantum dot; ligand



Citation: Welyab, G.; Abebe, M.; Mani, D.; Thankappan, A.; Thomas, S.; Aga, F.G.; Kim, J.Y. All-Inorganic CsPbBr₃ Perovskite Nanocrystals Synthesized with Olive Oil and Oleylamine at Room Temperature. *Micromachines* **2023**, *14*, 1332. <https://doi.org/10.3390/mi14071332>

Academic Editors: Aiqun Liu and Alberto Tagliaferro

Received: 9 June 2023

Revised: 24 June 2023

Accepted: 28 June 2023

Published: 29 June 2023



Copyright: © 2023 by the authors. Licensee MDPI, Basel, Switzerland. This article is an open access article distributed under the terms and conditions of the Creative Commons Attribution (CC BY) license (<https://creativecommons.org/licenses/by/4.0/>).

1. Introduction

Halide perovskites (HPs) have the general chemical structure of ABX₃, where A (methylammonium (MA) CH₃NH₃⁺, formamidinium (FA) CH(NH₂)₂⁺, methylhydrazinium CH₃(NH₂)₂⁺, aziridinium (CH₂)₂NH₂⁺ and cesium Cs⁺) and B (lead Pb²⁺, tin Sn²⁺, and germanium Ge²⁺) are cations, and X (chlorine Cl⁻, bromine Br⁻, and iodine I⁻) is an anion [1–7]. When these HPs serve as a semiconducting layer for the electronic and optoelectronic devices, they share some common properties such as defect tolerance, large absorption coefficient, high dielectric constant, low exciton binding energy, long charge carrier diffusion length, high charge mobility, and tunable bandgap [8–13]. Hence, the state-of-the-art devices show the power conversion efficiency of ~26% for photovoltaic (PV) cells, and more than 20% quantum efficiency for light-emitting diodes (LEDs) [4,14–17]. Furthermore, based on the excellent aforementioned properties, HPs have been applied to lasers, photodetectors, X-ray/ γ -ray detectors, medical imaging devices, biosensors, photocatalysis, and luminescence solar concentrators [18–25]. However, the organic–inorganic hybrid HPs have an intrinsic problem in thermal stability originating from the organic cations such as MA and FA in the perovskite structure [26,27]. For example, MABr decomposes at around

250–350 °C [27]. Hence, to overcome this thermal instability, all-inorganic HPs such as CsPbX_3 ($X = \text{Cl, Br, and I}$) have been employed for perovskite electronics [27–34].

However, it is notable that all-inorganic Cs-based perovskites with a wide bandgap ($E_g > 1.65$ eV) [35,36] also have some stability issues. First, the Goldschmidt tolerance factor (t) is $(r_A + r_X) / \{\sqrt{2} \cdot (r_B + r_X)\}$, in which r_A , r_B , and r_X are the radius of cation A, cation B, and anion X, respectively [37]. In the case of CsPbCl_3 , CsPbBr_3 , and CsPbI_3 , each tolerance factor is 0.87, 0.816, and 0.805, respectively [38,39]. Considering that the cubic phase could be stable in the range of $0.813 \leq t \leq 1.107$ [37], CsPbI_3 is structurally unstable among the cesium lead halides. Second, the Cs-based perovskites undergo a multiple polymorph transition, such as orthorhombic, tetragonal, and cubic, depending on the temperature and composition [40]. To be a thermodynamically stable cubic phase with high symmetry, the perovskite should stay at the temperature more than 47 °C for CsPbCl_3 , 130 °C for CsPbBr_3 , and 300 °C for CsPbI_3 , indicating that CsPbI_3 is the most challenging compound in spite of its promising energy bandgap ~ 1.73 eV [41–44]. Note that CsPbCl_3 and CsPbBr_3 each have a bandgap of ~ 3.03 eV and ~ 2.25 eV, respectively [45]. Furthermore, it is notable that CsPbI_3 undergoes a phase transition from the black γ -phase to the yellow δ -phase (i.e., a non-perovskite structure with $E_g \sim 2.82$ eV), resulting in an undesirable compound for perovskite electronics [46]. Third, according to Li and coworkers, the thermal stability of Cs-based perovskites is in the sequence of $\text{CsPbCl}_3 > \text{CsPbBr}_3 > \text{CsPbI}_3$. This is because the structural change was observed at 500 °C for CsPbCl_3 , 400 °C for CsPbBr_3 , and 200 °C for CsPbI_3 , respectively, which is based on in situ X-ray diffraction experiments as a function of temperature in ambient conditions [47,48]. Hence, we notice that CsPbCl_3 and CsPbBr_3 are superior to CsPbI_3 from the stability point of view. In this work, we may focus on the green-emitting CsPbBr_3 perovskite semiconductor [49,50].

In 1958, Møller reported the structure and photoconductivity of CsPbX_3 crystals ($X = \text{Cl, Br, and I}$) [28]. Then, after more than five decades, in 2015, Kovalenko and coworker invented a hot injection (HI) method for synthesizing CsPbX_3 ($X = \text{halide or its mixture}$) colloidal quantum dot materials with oleic acid (OA) and oleylamine (OAm) surface ligands [51]. Then, after one year, Zeng and coworker invented another method called supersaturated recrystallization (SR) for synthesizing CsPbX_3 nanocrystals (NCs) with OA and OAm at room temperature [52]. In 2019, Shi and coworker tried to replace OA with an edible ‘olive oil (OO)’ using the HI method [53]. Then recently, Jing and coworker tried to replace OA with another ligand called 4,4'-Azobis(4-cyanovaleric acid) (CA) at room temperature because OA and OAm can be detached easily from the surface of CsPbX_3 [54]. On the other hand, in 2022, Ray and coworkers proposed a new technique to synthesize CsPbX_3 ($X = \text{I/Br}$) by modifying the ligand chemistry using olive oil [55].

For fabricating a relatively more stable cubic phase of CsPbX_3 , there are three methods: (1) the synthesis of NCs with high surface energies, (2) surface ligand engineering, and (2) composition engineering [51–55]. These methods have been commonly utilized for synthesizing CsPbX_3 QDs. Hence, the colloidal CsPbX_3 NCs have several strong advantages compared to its bulk counterparts. First, based on quantum size and confinement effect, the energy bandgap of QD materials is easily tunable resulting in the full-color spectrum coverage. Second, the NC–ligand complexes can afford versatile solution processes via colloidal chemistry. Third, the perovskite NCs can enhance their optical properties, resulting in a high photoluminescence quantum yield (PLQY) and a narrow full width at half maximum (FWHM) for color purity, which is desirable for lighting and display applications [51,52].

In this study, we tried to replace OA with OO to synthesize CsPbBr_3 NCs at room temperature for which we adopted the SR method. To the best of authors' knowledge, in the past, the OO ligand was tested only by the HI method [53], although OO is promising as a surface ligand for the mass production process in future. Hence, in this work, we employed this OO ligand for synthesis of CsPbBr_3 NCs at room temperature. Note that SR is a type of ligand-assisted reprecipitation (LARP) technique, affording a simple, low cost, and a large production capability in ambient conditions. Furthermore, basically, SR is an antisolvent-mediated solution process, resulting in the nucleation and growth of perovskite

NCs. Hence, the classical LaMer model [56,57] and solvent engineering (SE) [58,59] should be very important for addressing the SR mechanism in the synthesis of CsPbBr₃ NCs at room temperature.

2. Materials and Methods

2.1. Chemicals

Lead bromide (PbBr₂, 99.0%, AR chemicals, Delhi, India), cesium bromide (CsBr, 99.9%, Sigma-Aldrich, Darmstadt, Germany), oleic acid (OA, 98%, Sigma-Aldrich, Darmstadt, Germany), oleylamine (OAm, technical grade 70%, Sigma-Aldrich, Darmstadt, Germany), olive oil (OO, Nice, Kochi, India), hexane ($\geq 97.5\%$, Sigma-Aldrich, Darmstadt, Germany), *N,N*-dimethylformamide (DMF, 99.5%, AR chemicals, Delhi, India), and toluene ($\geq 99.5\%$, AR chemicals, Delhi, India) were used in this experiment. All chemicals were used without further purification.

2.2. Synthesis of CsPbBr₃ Nanocrystals

In the SR method [52], the perovskite precursors and ligands, CsBr (0.2 mmol, 43 mg), PbBr₂ (0.2 mmol, 73 mg), OA or OO (0.5 mL), and 0.25 mL of oleylamine, were dissolved into 5 mL of a polar DMF solvent and stirred using magnetic stirrers at RT for two hours. Then, 1 mL of the perovskite precursor solution was titrated into 10 mL of a nonpolar toluene antisolvent and stirred for 60 s. Then, the CsPbBr₃ NC dispersion exhibited a green-light emission under 365 nm UV illuminations, confirming that the reaction was successful through the SR method. Then, this colloidal dispersion was transferred to a centrifuge tube for centrifugations, and it was centrifuged at 8000 rpm for 10 min. The supernatant was discarded, and the resulting precipitate was re-dispersed in the nonpolar hexane. Then, the final CsPbBr₃ sample was dried under a vacuum oven at 60 °C overnight. Finally, the CsPbBr₃ samples were kept for further characterization at RT.

2.3. Characterization

The structural properties of CsPbBr₃ (OA and OAm) and CsPbBr₃ (OO and OAm) were determined by the X-ray diffraction (XRD) measurements measured using the Rigaku mini flex-300/600 diffractometer (Tokyo, Japan). The irradiation used CuK α , $\lambda = 1.5406 \text{ \AA}$ at 40 kV and 15 mA for the XRD analysis. The CsPbBr₃ NC's size and shape were determined by using the high-resolution transmission electron microscopy (HR-TEM) (Model: JEOL, JEM-2100) with an operating voltage of 200 kV. The optical absorption was characterized by using the Ultraviolet-visible (UV-vis) absorption spectroscopy (SHIMADZU UV-2600, Kyoto, Japan), whereas the photoluminescence (PL) spectra were measured using a spectrophotometer (SHIMADZU RF-6000, Kyoto, Japan) at the excitation wavelength of 375 nm. The Fourier transform infrared spectroscopy (FT-IR) analysis was performed by using the PerkinElmer Spectrum Two FT-IR Spectrometer. For this purpose, the attenuated total reflection (ATR) was employed as a sampling technique to record the FT-IR spectra of the drop-cast CsPbBr₃ thin film in the range 4000–400 cm⁻¹ with resolution of 4 cm⁻¹. Here, for the drop-cast thin films, the glass substrate was washed in detergent soap, followed by ultra-sonication using distilled water, acetone, and isopropanol, respectively, for 15 min per each process. Then, the cleaned substrate was dried at 80 °C for 1 h in vacuum oven and subsequently cooled down at room temperature. The prepared sample solution (10 mg perovskite precursors in 1 mL of toluene) was drop cast on the clean glass substrate and dried in ambient conditions. The PL decay curves were recorded by using a time-correlated single photon counting (TCSPC) (Model: Fluorolog 3 TCSPC, Horiba, Irvine, CA, USA).

2.4. Computational Methods

The electronic band structures of the CsPbBr₃ unit cell were calculated using the Cambridge Serial Total Energy Package (CASTEP, Materials Studio 2017) software with the density functional theory. The Perdew–Burke–Ernzerhof (PBE) parametrization of the General Gradient Approximation (GGA) was used to describe the exchange correla-

tion functional. The unit cell in the Brillouin zone was applied to evaluate the electronic band structures. Energy of 5×10^{-5} eV/atom, maximum force of 0.01 eV/Å, maximum displacement of 5×10^{-4} Å, and maximum stress of 0.02 GPa were used for all geometry optimization.

3. Results and Discussion

Figure 1a shows the orthorhombic structure (space group, $Pbnm$) of CsPbBr_3 crystal. However, when temperature increased, CsPbBr_3 undergoes a phase transition from orthorhombic to tetragonal ($P4/mbm$) at 88 °C and from tetragonal to cubic ($Pm\bar{3}m$) at 130 °C through a tiny rearrangement of the unit cell atoms [60,61]. On the other hand, in the case of NCs, the unit cell structure could be affected not only by crystal size/shape, but also by the Pb^{2+} /ligand ratio [34]. For example, the cubic phase was observed at RT if the crystal size is in nanoscale, indicating the metastable state of NCs. In the case of the electronic structures of CsPbBr_3 unit cell, the information could be found in the Supplementary Materials (SM), Figure S1, displaying that the bandgap (E_g) is reduced with from 2.40 eV (cubic) to 2.31 eV (orthorhombic) via 2.37 eV (tetragonal).

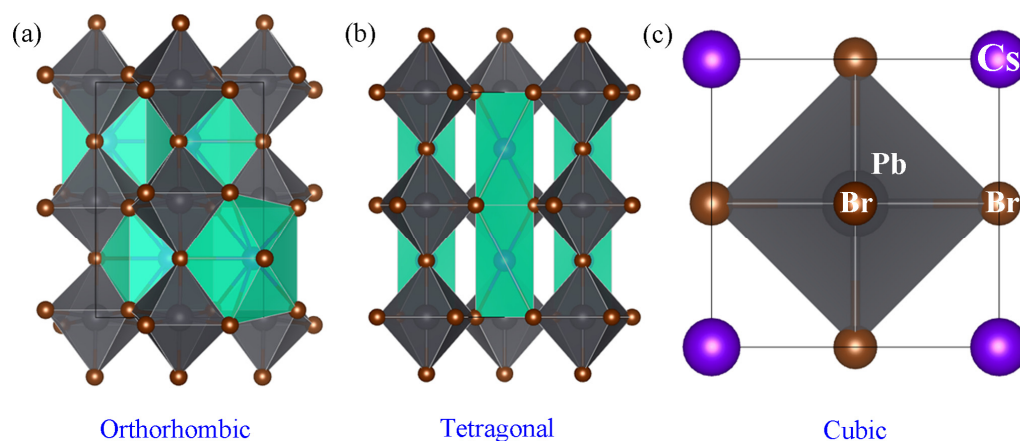


Figure 1. Polyhedral of CsPbBr_3 unit cell: (a) orthorhombic, (b) tetragonal, and (c) cubic structure.

Figure 2 shows the chemical structure of (a) OO, (b) OAm, and (c) DMF and toluene, among which both organic OO and OAm surface ligands were employed as a mixed ligand for the synthesis of CsPbBr_3 at RT using the SR process [52]. As shown in Figure 2a, the OO's glycerol fractions ($\sim 98\%$ of total OO) are composed of oleic acid, linoleic acid, palmitic acid, and palmitoleic acid, but it also contains small amounts of non-glycerol fraction ($\sim 1\text{--}2\%$ of the total OO by weight), such as biophenols and triterpenic acids [62]. Here, because of the conformational freedom (e.g., a chain folding) of the C-C single-bond rotation, the high carbon ligand may undergo a chain folding in a typical solvent medium, DMF. Importantly, it is noteworthy that the compositional engineering (or mixing strategy) has been commonly used for perovskite electronics for enhancing stability, e.g., cation mixtures (MA^+/FA^+), metal ion mixtures ($\text{Pb}^{2+}/\text{Sn}^{2+}$ or $\text{Ge}^{2+}/\text{Sn}^{2+}$), halogen mixtures ($\text{Cl}^-/\text{Br}^-/\text{I}^-$), perovskite dimensional mixtures (2D/3D), etc., which resulting in the enhancement of stability of materials and devices [62–67]. In the same vein, when we use the edible OO as a surface ligand, it might be useful in stability with a guaranteed benefit of eco-friendliness, which is a desirable characteristic for a mass production process in future.

Figure 3a shows the free energy change (ΔG) as a function of the radius (r) when the nucleus is assumed to be a spherical according to the LaMer model, a classical nucleation theory [56,57]. Here, the free energy change (ΔG_{hom}) for homogenous nucleation and that (ΔG_{het}) for heterogeneous nucleation could be defined as follows,

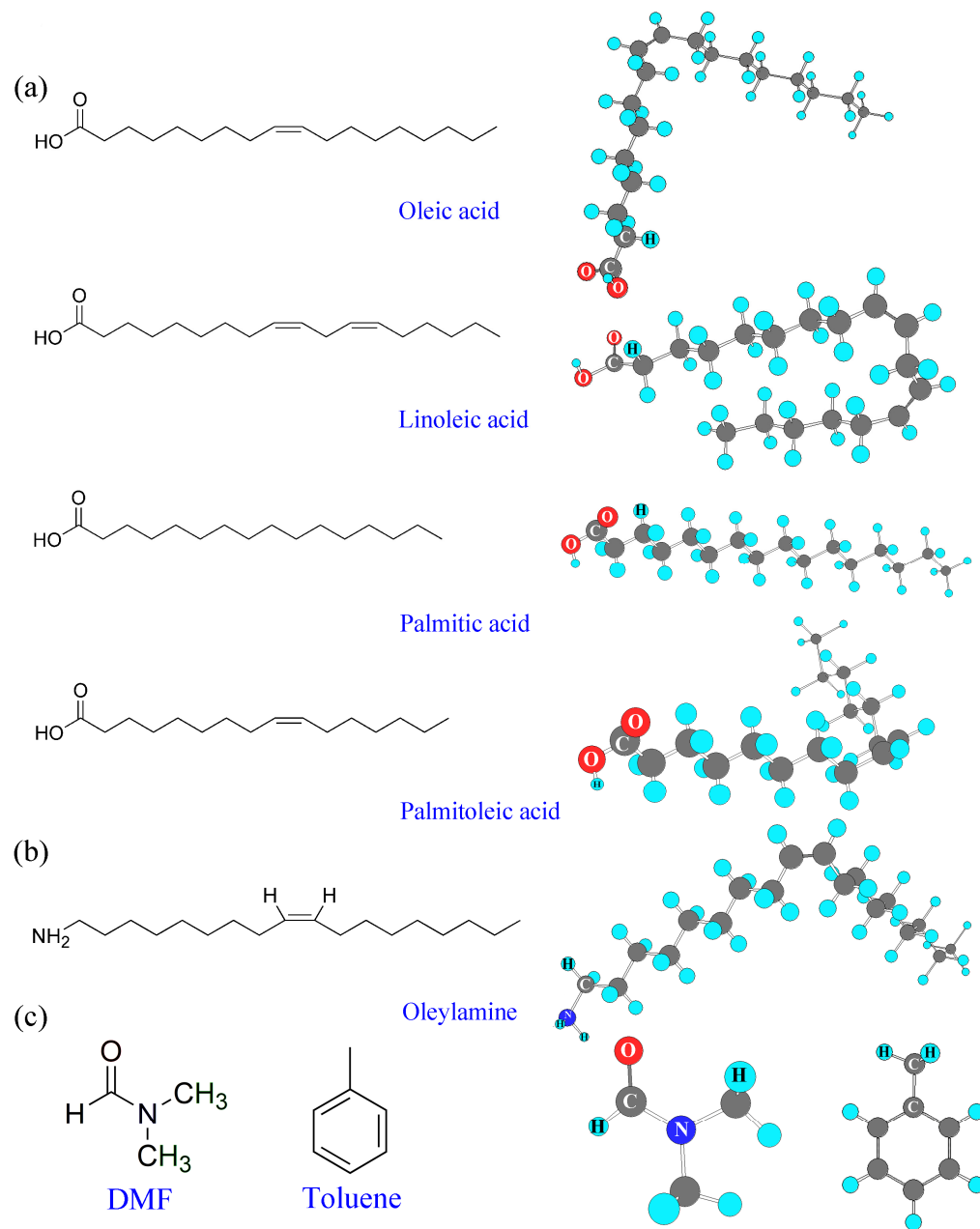


Figure 2. Chemical structures of (a) olive oil: glycerol fractions, ~98%; (b) oleylamine; and (c) DMF and toluene.

$$\Delta G_{hom} = -\frac{4}{3}\pi r^3 \Delta G_v + 4\pi r^2 \gamma_{SL} \quad (1)$$

$$\Delta G_{het} = \left\{ -\frac{4}{3}\pi r^3 \Delta G_v + 4\pi r^2 \gamma_{SL} \right\} \cdot \frac{(2 + \cos \theta)(1 - \cos \theta)^2}{4} \quad (2)$$

where ΔG_v is the free energy change associated with the formation of a small volume of solid, whereas γ_{SL} is the solid/liquid interfacial free energy. Furthermore, $\Delta G_{het} = \Delta G_{hom} \cdot S(\theta)$, where $S(\theta) = (2 + \cos \theta)(1 - \cos \theta)^2/4$ is a shape factor at a wetting angle θ . According to the LaMer model [57], when a solution is supersaturated by undercooling, a nucleus could be formed. If this nucleus is larger than the critical size (r^*), the spontaneous growth is available because ΔG is decreasing as shown in Figure 3a (see the blue solid line). In the case of the SR process, a supersaturated condition is directly available when the perovskite precursor solution (a colloidal dispersion containing bromide plumbate, $PbBr_n^{2-n}$ with $n = 2-6$) is dropped into

the antisolvent medium, e.g., toluene with Gutmann's number (D_N) ~ 0.1 kcal/mol, i.e., Lewis basicity (see Table 1 for details) [68]. Here, it is noteworthy that a nonpolar toluene with solubility parameter, $\delta = 8.9$ (cal/cm³)^{1/2} is antisolvent for the bromide plumbate but it is still miscible with the polar DMF solvent ($\delta = 12.1$ (cal/cm³)^{1/2}) [69], indicating that the perovskite precursor ions (Cs⁺, Pb²⁺, Br⁻) will be directly exposed to the antisolvent toluene molecules, resulting in the nucleation and growth of perovskite NCs as explained through the critical point (r^*-G^*) in the LaMer model. However, it is notable that in the case of SR process, the supersaturation was reached simply by adding the precursor solution into the antisolvent (not by undercooling like in the LaMer model). Interestingly, the SR process is similar to the well-known Solvent Engineering (SE) (i.e., one-step antisolvent method) in the sense that the wet precursor solution is directly exposed to the antisolvent molecules [58,59]. However, the difference is that the SE method is processed during the spin-coating step by dispensing the antisolvent on the top of a wet precursor solution. Furthermore, SE allows for the formation of intermediate phase when a polar solvent DMSO is employed, whereas SR may not allow for it because the colloidal dispersion may undergo a direct crystallization (at least without a co-solvent such as DMSO). Importantly, the SR process corresponds to the heterogeneous nucleation and growth of CsPbBr₃ perovskite because the nanoscale crystallization was processed through the surface of haloplumbate dispersed in the DMF medium. Recall that the perovskite precursor solution is a typical colloidal dispersion [70], i.e., haloplumbate is dispersed in a solvent medium, herein DMF with $D_N = 26.6$ kcal/mol. In the case of Br⁻, its D_N is 33.7 kcal/mol [71], indicating that Pb²⁺ (Lewis acid) may have a stronger coordination bonding with Br⁻ ions (Lewis base) than DMF to form the acid–base adducts in spite that DMF is a good solvent for the perovskite precursor materials. See Figure S2 in the Supplementary Materials for the vials containing CsPbBr₃ NCs in the supersaturated solution/dispersion.

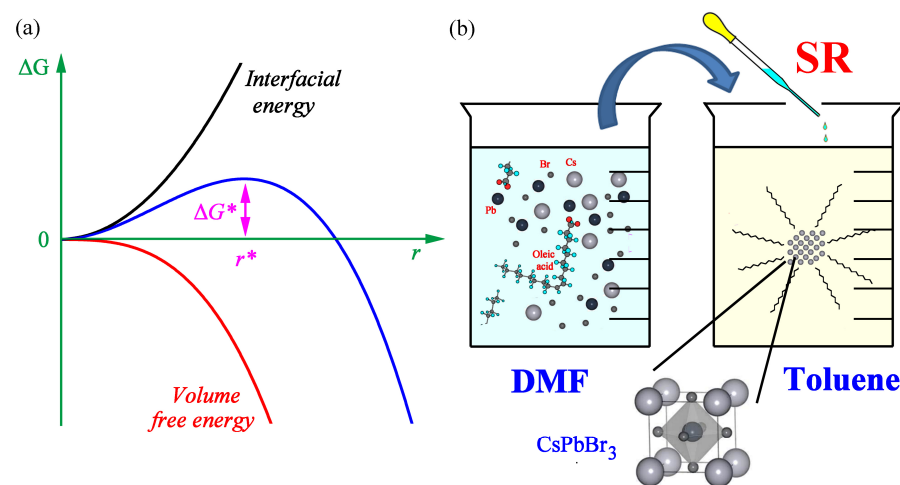


Figure 3. (a) The free energy change (ΔG) in the nucleation and growth process as a function of r (a radius of a spherical nucleus by assumption). Here, ΔG^* is the critical free energy barrier at the critical radius (r^*), where a unit cell is formed. (b) Schematic explanation of supersaturated recrystallization (SR) of CsPbBr₃ in the antisolvent toluene.

Table 1. Gutmann's solvent donor number (D_N), solubility parameter (δ), dielectric constant (ϵ), molar mass, density, and boiling point (b.p.), and the chemical structures of solvents.

Solvent	D_N (kcal/mol)	δ^1 (cal/cm ³) ^{1/2}	ϵ	Molar Mass (g/mol)	Density (g/cm ³)	b.p. (°C)	Chemical Structure
DMF	26.6	12.1	36.1	70.095	0.948	153	C ₃ H ₇ NO
Toluene	0.1	8.9	2.38	92.140	0.867	111	C ₆ H ₅ CH ₃

¹ In MKS unit, the δ value is 24.8 MPa^{1/2} for DMF and 18.2 MPa^{1/2} for toluene, respectively.

Figure 4a,b show the experimental XRD patterns for the drop-cast CsPbBr₃ thin film on the glass substrate depending on the surface ligand species: (Figure 4a) OA and OAm and (Figure 4b) OO and OAm, whereas Figure 4c,d shows the XRD patterns for (Figure 4c) cubic and (Figure 4d) orthorhombic based on Joint Committee on Powder Diffraction Standards (JCPDS). As shown in Figure 4a–c, the location of XRD peaks such as (100), (110), and (200) are more corresponding to that of cubic (JCPDS: PDF#96-153-0682: space group $Pm\bar{3}m$) instead of orthorhombic in spite that it was synthesized at RT [29,55,72,73]. Note that the lattice constant is 5.6050 Å based on the above JCPDS data, which was confirmed by the *d*-spacing of ~5.478 Å or 5.418 Å = $\lambda / (2 \cdot \sin \theta)$ at $\theta = 8.08^\circ$ (OA) or 8.17° (OO), respectively, when the X-ray wavelength (λ) is 1.5406 Å. Probably, the CsPbBr₃ NC may prefer to exist in cubic phase due to its high surface energy and capping ligand effects. Furthermore, all the drop-cast CsPbBr₃ nanocrystalline thin films on the glass substrate display two intense peaks at $2\theta = 16^\circ$ and 32° , corresponding to (100) and (200) crystallographic planes, respectively, indicating that there is orientational order to the (100) direction. However, when the OO and OAm ligands were incorporated as a ligand system for CsPbBr₃, the additional (110) peak is clearly observed, indicating that the mixed ligand system by OO's glycerol fraction makes the orientational order be reduced, resulting in a partial amorphous halo (see the baseline shape centered around (110) peak). However, when we estimated the crystallite size (*t*) by Scherrer equation (Equation (3)), it was in the range of ~40–42 nm for all the samples (Table 2).

$$t = \frac{0.9 \cdot \lambda}{B \cdot \cos \theta} \quad (3)$$

where λ (= 0.154 nm) is the X-ray wavelength, and *B* is the full width at half maximum (FWHM) at the angle θ . Here, it is noteworthy is that the estimated crystallite size is a direct particle size of this single crystal in nanoscale, which will be further addressed in the below section.

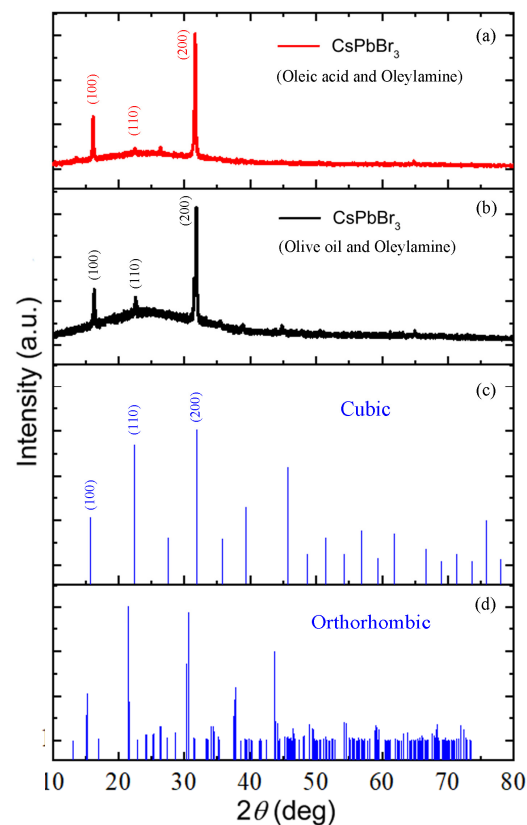


Figure 4. XRD patterns of CsPbBr₃ nanocrystal drop-cast thin film depending on the ligand species: (a) oleic acid and oleylamine and (b) olive oil and oleylamine. (c) Joint Committee on Powder Diffraction Standards (JCPDS) (PDF#96-153-0682) and (d) JCPDS (PDF#96-153-3063).

Table 2. Crystallite size (t) of CsPbBr₃ at the (200) crystallographic plane. Here, β denotes a full width at half maximum (FWHM).

CsPbBr ₃ Nanocrystals					
	Crystal Planes	2θ (°)	θ (°)	β (Radian)	t (nm)
Oleic Acid (OA)	(100)	16.15	8.08	0.003323	42
	(200)	31.65	15.83	0.003641	40
Olive Oil (OO)	(100)	16.33	8.17	0.003438	41
	(200)	31.80	15.90	0.003438	42

Figure 5 shows HR-TEM images for CsPbBr₃ depending on the surface ligand system. Figure 5a,b show the case of OA and OAm, whereas Figure 5c,d show the case of OO and OAm. As shown in Figure 5, the TEM images show roughly a nano cubic, which is in line with the XRD data exhibiting the cubic structure.

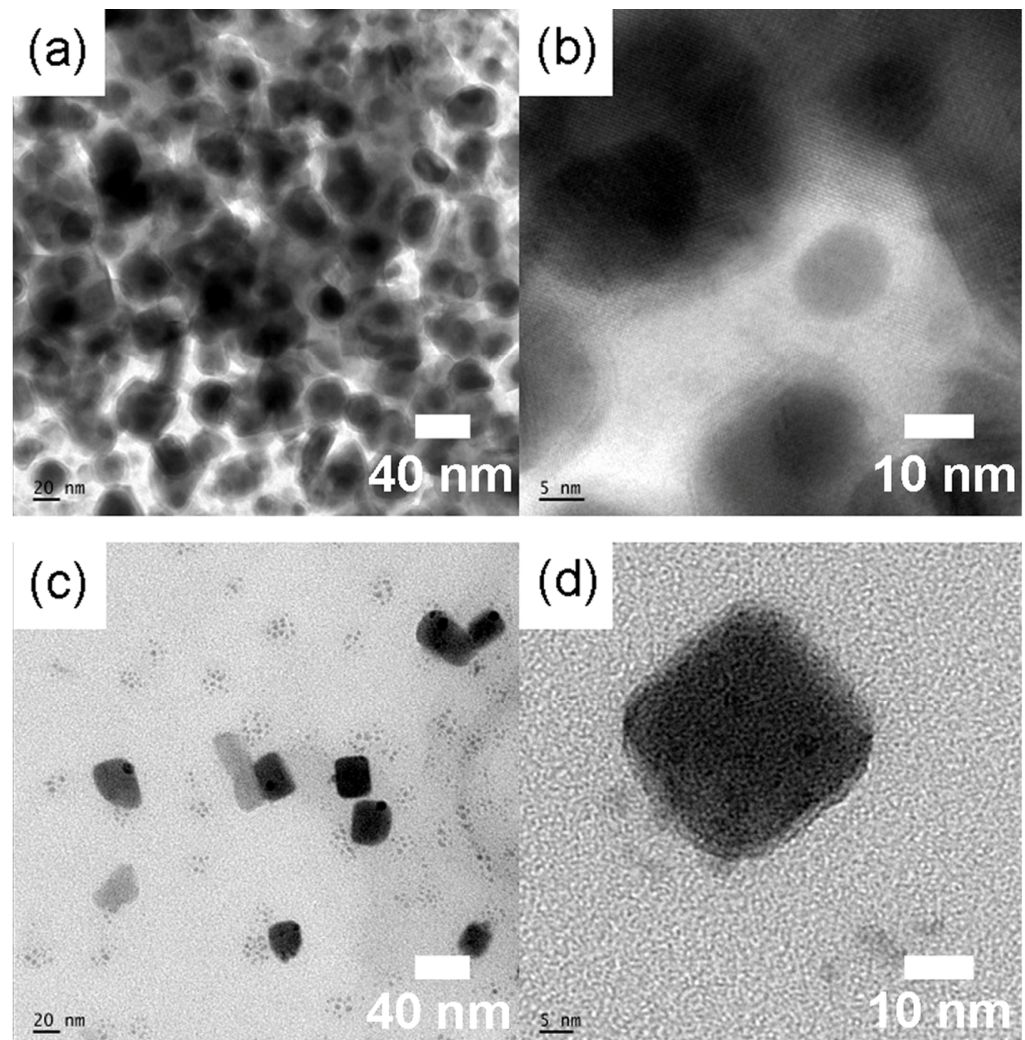


Figure 5. HR-TEM images of CsPbBr₃ nanocrystals (nano cubic) when the ligand was oleic acid and oleylamine (a,b) and olive oil and oleylamine (c,d).

Figure 6 shows (a) the UV-vis absorption and (b) the PL emission spectra for the two different colloidal dispersions containing CsPbBr₃ NCs depending on the ligand species. Here, it is noteworthy that the CsPbBr₃ perovskite is a direct semiconductor. In addition, the synthesized CsPbBr₃ NCs do not display any grain boundary in Figure 5, indicating a single crystalline nature in nanoscale although there might be some surface

defects. Therefore, the CsPbBr₃ NCs are different from the disordered conjugated polymers showing a localized state. For disordered system, Mott defined a mobility edge between localized and delocalized states [74]. However, in the case of CsPbBr₃ NCs, the sharp absorption edge is expected, affording the decision of optical bandgap by using a simple tangential slope based on the equation, $E = hc/\lambda$, where E is energy, h is Planck's constant, c is the speed of light, and λ is the wavelength of light. Therefore, according to the UV-Vis absorption edge (530 nm vs. 533 nm) in Figure 6a, the corresponding optical bandgap (E_g) is 2.34 eV = 1240/530 (for OA and OAm) and 2.33 eV = 1240/533 (for OO and OAm), respectively. See Equation (4) for the conversion factor, 1240, between the energy (bandgap) and the wavelength (absorption edge).

$$\lambda[\text{nm}] = \frac{hc}{E} = \frac{(6.62607 \times 10^{-34} \text{ J} \times \text{s}) \times (3 \times 10^8 \text{ m/s}) (10^{-9} \text{ nm/1 m})}{E_g(\text{eV}) \times (1.60218 \times 10^{-19} \text{ J/1 eV})} = 1240 \frac{1}{E[\text{eV}]} \quad (4)$$

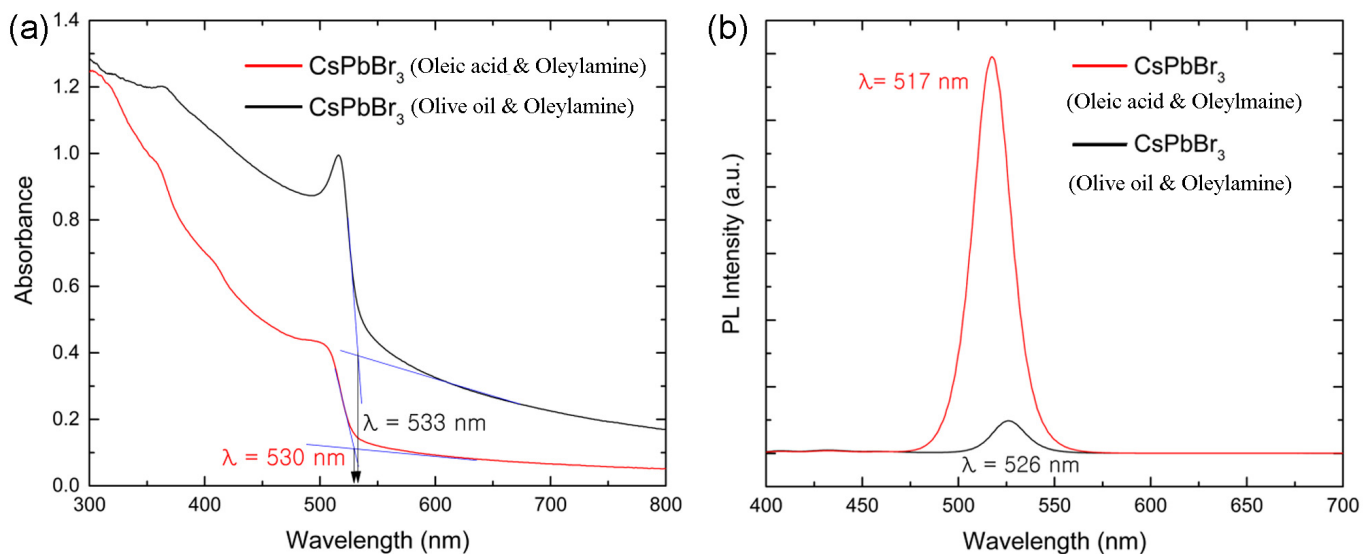


Figure 6. (a) UV-Vis absorbance spectra of the CsPbBr₃ nanocrystal dispersion depending on the ligand species. Here, $\lambda = 530$ nm corresponds to $E_g \approx 2.34$ eV (oleic acid and oleylamine) and $\lambda = 533$ nm corresponds to $E_g \approx 2.33$ eV (olive oil and oleylamine). (b) PL spectra of CsPbBr₃ nanocrystals depending on the ligand species.

This result indicates that the nanoparticle size might be slightly larger in CsPbBr₃ synthesized with OO and OAm. This result is in line with the estimated crystallite size trend according to the sharpest peak at the (200) crystallographic plane in Figure 4a and Table 2. On the other hand, the PL spectra exhibit the PL peak at 517 nm for CsPbBr₃ with oleic acid and oleylamine and at 526 nm for CsPbBr₃ with OO and OAm. Here, the shift of PL peak from 517 nm to 526 nm (a red shift) indicates that the effective crystal size (or aggregation) of CsPbBr₃ NCs is slightly larger in the colloidal dispersion state when OO and OAm were employed as the surface ligands, although the apparent size (Table 2) is similar for both ligand systems in the solid state. Furthermore, it is believed that the surface state of NCs is different depending on the NC–ligand complexations. Hence, when OO and OAm were complexed with CsPbBr₃ NCs, there might be more surface defects, resulting in more non-radiative recombination (i.e., smaller PL intensity) in Figure 6b. Furthermore, FWHM is 21 nm for the former, but 19 nm for the latter. According to our finding, the narrow emission spectra were obtained below 25 nm, which falls in the required range of 12–42 nm [51] for the optoelectronic applications such as lighting and display technology.

Figure 7a shows PL decay curve for the colloidal CsPbBr₃ NC dispersion as a function of ligand species. The average lifetime of electron–hole pairs (Wannier–Mott excitons) is 1.167 ns for CsPbBr₃ with OA and OAm, whereas it is 3.228 ns for CsPbBr₃ with OO and OAm, indicating that a slightly larger CsPbBr₃ with OO and OAm displays a longer life time

of excitons. Figure 7b shows the FT-IR spectra for the drop-cast CsPbBr₃ nanocrystalline thin film. First of all, the IR spectrum for CsPbBr₃ with OA and OAm is relatively simpler than that for CsPbBr₃ with OO and OAm. Second, the FT-IR spectrum for OO and OAm shows a high absorption at 3020–2850 cm⁻¹, whereas the corresponding spectrum for OA and OAm is very weak at those wavenumbers, which correspond to the symmetric and asymmetric C-H stretching modes [53,54]. The functional groups of other organic components can be attributed to the absorption peaks at 3781 cm⁻¹ [54] and 3510 cm⁻¹ [53], which originate from the N-H characteristic absorption. The IR peaks at around 1800–1600 cm⁻¹ are related to carbonyl (C=O) mode of stretching vibration which can be shift to lower wavenumber due to any perturbation. The shift of wavenumber may be ascribed to the presence of hydrogen bonding. The peaks at 1538 cm⁻¹ and 1462 cm⁻¹ are related to C-CH₃ asymmetric bending. On the other hand, the peaks at 1377 cm⁻¹ and 1262 cm⁻¹ correspond to C-CH₃ symmetric bending vibration and C-N stretching vibration, respectively. Absorption peaks in the range of 1000–500 cm⁻¹ indicate that the existence of aromatic bending vibrations [75], which might originate from OO components, trapped toluene (C₆H₅CH₃), and/or aromatic impurities in samples. The peak at 477–447 cm⁻¹ is associated with CsPbBr₃-OAm complexes [76].

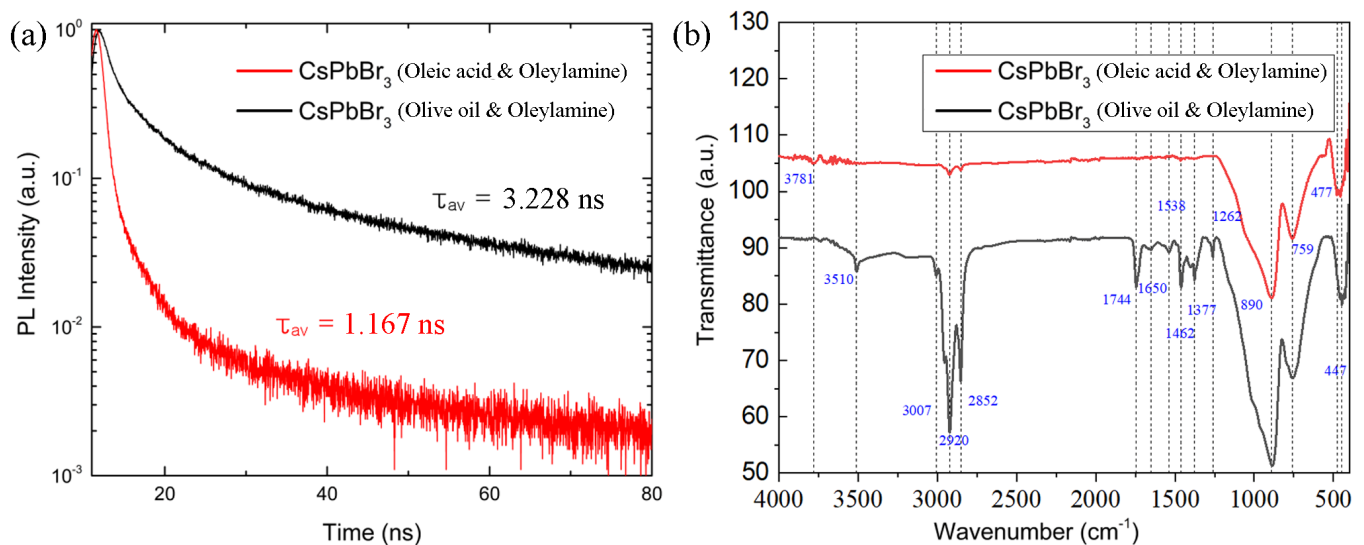


Figure 7. (a) PL spectra decay of CsPbBr₃ nanocrystals depending on the ligand species. (b) FT-IR spectra of CsPbBr₃ nanocrystals depending on the ligand species.

4. Conclusions

In this work, we demonstrated the usefulness of olive oil and oleylamine as the surface ligand system (vs. the typical oleic acid and oleylamine mixtures) for the synthesis of CsPbBr₃ nanocrystals at room temperature. For this purpose, the supersaturated recrystallization process was employed, enabling a direct synthesis of perovskite nanocrystals. First, according to XRD, the crystallite size is ~40–42 nm in both conditions (oleic acid and oleylamine vs. olive oil and oleylamine), whereas the latter system allows for a less orientational order than the former by showing a partial amorphous halo. The TEM images confirmed that the CsPbBr₃ nanocrystals have a cuboid shape in line with XRD data exhibiting a cubic phase. The UV-Vis absorption data exhibited that the optical bandgap of CsPbBr₃ is about 2.3 eV in both ligand systems. The PL emission spectra indicated that FWHM is about 19 nm (olive oil and oleylamine) vs. 21 nm (oleic acid and oleylamine), which falls into the desirable FWHM values, i.e., ~12–42 nm for technical applications. Finally, the average PL lifetime is 3.228 ns for olive oil and oleylamine and 1.167 ns for oleic acid and oleylamine. Future work may include the application of CsPbBr₃ nanocrystals to the biosensors and optoelectronic devices.

Supplementary Materials: The following are available online at: <https://www.mdpi.com/article/10.3390/mi14071332/s1>, Figure S1: The electronic structures of CsPbBr₃ unit cells displaying polymorphism: (a) orthorhombic, (b) tetragonal, and (c) cubic phase. Here, the bandgap energy (E_g) of each unit cell is 2.31 eV for orthorhombic, 2.37 eV for tetragonal, and 2.40 eV for cubic phase, respectively. Figure S2: Vials containing a CsPbBr₃ colloidal dispersion depending on surface ligands: (a) oleic acid and oleylamine—a normal photo, (b) oleic acid and oleylamine—under 365 nm UV light, (c) olive oil and oleylamine—a normal photo, and (d) olive oil and oleylamine—under 365 nm UV light. Hence, CsPbBr₃ nanocrystals can serve as a green-light emitter.

Author Contributions: Writing—original draft preparation, G.W.; writing—review and editing, J.Y.K.; conceptualization, G.W., M.A., D.M., A.T., S.T. and J.Y.K.; methodology, G.W. and J.Y.K.; software, G.W. and F.G.A.; formal analysis and investigation, G.W. and J.Y.K.; resources, S.T.; data curation, G.W.; supervision and project administration, M.A., D.M., A.T., S.T. and J.Y.K. All authors have read and agreed to the published version of the manuscript.

Funding: This research received no external funding.

Data Availability Statement: The datasets used and/or analyzed during the current study are available from the corresponding author upon reasonable request.

Acknowledgments: Jimma University and Mizan-Tepi University are acknowledged for supporting G.W.

Conflicts of Interest: The authors declare no conflict of interest.

References

1. Kojima, A.; Teshima, K.; Shirai, Y.; Miyasaka, T. Organometal halide perovskites as visible-light sensitizers for photovoltaic cells. *J. Am. Chem. Soc.* **2009**, *131*, 6050–6051. [[CrossRef](#)] [[PubMed](#)]
2. Lee, M.M.; Teuscher, J.; Miyasaka, T.; Murakami, T.N.; Snaith, H.J. Efficient Hybrid Solar Cells Based on Meso-Superstructured Organometal Halide Perovskites. *Science* **2012**, *338*, 643–647. [[CrossRef](#)] [[PubMed](#)]
3. Stranks, S.D.; Eperon, G.E.; Grancini, G.; Menelaou, C.; Alcocer, M.J.P.; Leijtens, T.; Herz, L.M.; Petrozza, A.; Snaith, H.J. Electron-Hole Diffusion Lengths Exceeding 1 Micrometer in an Organometal Trihalide Perovskite Absorber. *Science* **2013**, *342*, 341–344. [[CrossRef](#)]
4. Min, H.; Kim, M.; Lee, S.-U.; Kim, H.; Kim, G.; Choi, K.; Lee, J.H.; Seok, S.I. Efficient, stable solar cells by using inherent bandgap of a-phase formamidinium lead iodide. *Science* **2019**, *366*, 749–753. [[CrossRef](#)]
5. Zhou, Y.; Herz, L.M.; Jen, A.K.-Y.; Saliba, M. Advances and challenges in understanding the microscopic structure–property–performance relationship in perovskite solar cells. *Nat. Energy* **2021**, *7*, 794–807. [[CrossRef](#)]
6. Maćzka, M.; Ptak, M.; Gagor, A.; Stefańska, D.; Zaręba, J.K.; Sieradzki, A. Methylhydrazinium Lead Bromide: Noncentrosymmetric Three-Dimensional Perovskite with Exceptionally Large Framework Distortion and Green Photoluminescence. *Chem. Mater.* **2020**, *32*, 1667–1673. [[CrossRef](#)]
7. Stefańska, D.; Ptak, M.; Maćzka, M. Synthesis, Photoluminescence and Vibrational Properties of Aziridinium Lead Halide Perovskites. *Molecules* **2022**, *27*, 7949. [[CrossRef](#)]
8. Brivio, F.; Walker, A.B.; Walsh, A. Structural and electronic properties of hybrid perovskites for high-efficiency thin-film photovoltaics from first-principles. *APL Mater.* **2013**, *1*, 042111. [[CrossRef](#)]
9. Stoumpos, C.C.; Malliakas, C.D.; Kanatzidis, M.G. Semiconducting Tin and Lead Iodide Perovskites with Organic Cations: Phase Transitions, High Mobilities, and Near-Infrared Photoluminescent Properties. *Inorg. Chem.* **2013**, *52*, 9019–9038. [[CrossRef](#)]
10. Wolf, S.D.; Holovsky, J.; Moon, S.-J.; Löper, P.; Niesen, B.; Ledinsky, M.; Haug, F.-J.; Yum, J.-H.; Ballif, C. Organometallic Halide Perovskites: Sharp Optical Absorption Edge and Its Relation to Photovoltaic Performance. *J. Phys. Chem. Lett.* **2014**, *5*, 1035–1039. [[CrossRef](#)]
11. Manser, J.S.; Christians, J.A.; Kamat, P.V. Intriguing Optoelectronic Properties of Metal Halide Perovskites. *Chem. Rev.* **2016**, *116*, 12956–13008. [[CrossRef](#)] [[PubMed](#)]
12. Herz, L.M. Charge-Carrier Mobilities in Metal Halide Perovskites: Fundamental Mechanisms and Limits. *ACS Energy Lett.* **2017**, *2*, 1539–1548. [[CrossRef](#)]
13. Huang, J.; Yuan, Y.; Shao, Y.; Yan, Y. Understanding the physical properties of hybrid perovskites for photovoltaic applications. *Nat. Rev. Mater.* **2017**, *2*, 17042. [[CrossRef](#)]
14. Zhao, B.; Bai, S.; Kim, V.; Lamboll, R.; Shivanna, R.; Auras, F.; Richter, J.M.; Yang, L.; Dai, L.; Alsari, M.; et al. High-efficiency perovskite-polymer bulk heterostructure light-emitting diodes. *Nat. Photon.* **2018**, *12*, 783. [[CrossRef](#)]
15. Mathews, I.; Sofia, S.; Ma, E.; Jean, J.; Laine, H.S.; Siah, S.C.; Buonassisi, T.; Peters, I.M. Economically Sustainable Growth of Perovskite Photovoltaics Manufacturing. *Joule* **2020**, *4*, 822–839. [[CrossRef](#)]
16. Sun, C.; Jiang, Y.; Cui, M.; Qiao, L.; Wei, J.; Huang, Y.; Zhang, L.; He, T.; Li, S.; Hsu, H.-Y.; et al. High-performance large-area quasi-2D perovskite light-emitting diodes. *Nat. Commun.* **2021**, *12*, 2207. [[CrossRef](#)]

17. Park, J.; Kim, J.; Yun, H.-S.; Paik, M.J.; Noh, E.; Mun, H.J.; Kim, M.G.; Shin, T.J.; Seok, S.I. Controlled growth of perovskite layers with volatile alkylammonium chlorides. *Nature* **2023**, *616*, 724–730. [[CrossRef](#)]
18. Zhang, C.; Kuang, D.-B.; Wu, W.-Q. A Review of Diverse Halide Perovskite Morphologies for Efficient Optoelectronic Applications. *Small Methods* **2020**, *4*, 1900662. [[CrossRef](#)]
19. Pan, L.; Pandey, I.R.; Miceli, A.; Klepov, V.V.; Chung, D.Y.; Kanatzidis, M.G. Perovskite CsPbBr₃ Single-Crystal Detector Operating at 10¹⁰ Photons s⁻¹ mm⁻² for Ultra-High Flux X-ray Detection. *Adv. Optical. Mater.* **2023**, *11*, 2202946. [[CrossRef](#)]
20. Jeong, B.; Veith, L.; Smolders, T.J.A.M.; Wolf, M.J.; Asadi, K. Room-Temperature Halide Perovskite Field-Effect Transistors by Ion Transport Mitigation. *Adv. Mater.* **2021**, *33*, 2100486. [[CrossRef](#)]
21. Zhang, Q.; Shang, Q.; Su, R.; Do, T.T.H.; Xiong, Q. Halide Perovskite Semiconductor Lasers: Materials, Cavity Design, and Low Threshold. *Nano Lett.* **2021**, *21*, 1903–1914. [[CrossRef](#)] [[PubMed](#)]
22. Zhao, L.; Zhou, Y.; Shi, Z.; Ni, Z.; Wang, M.; Liu, Y.; Huang, J. High-yield growth of FACsPbBr₃ single crystals with low defect density from mixed solvents for gamma-ray spectroscopy. *Nat. Photon.* **2023**, *17*, 315–323. [[CrossRef](#)]
23. He, Y.; Petryk, M.; Liu, Z.; Chica, D.G.; Hadar, I.; Leak, C.; Ke, W.; Spanopoulos, I.; Lin, W.; Chung, D.Y.; et al. CsPbBr₃ perovskite detectors with 1.4% energy resolution for high-energy γ -rays. *Nat. Photon.* **2021**, *15*, 36–42. [[CrossRef](#)]
24. Zhang, X.; Peng, H.; Liu, J.; Yuan, Y. Highly sensitive plasmonic biosensor enhanced by perovskite-graphene hybrid configuration. *J. Opt.* **2023**, *25*, 075002. [[CrossRef](#)]
25. Huang, H.; Pradhan, B.; Hofkens, J.; Roeffaers, M.B.J.; Steele, J.A. Solar-Driven Metal Halide Perovskite Photocatalysis: Design, Stability, and Performance. *ACS Energy Lett.* **2020**, *5*, 1107–1123. [[CrossRef](#)]
26. Zhang, D.; Li, D.; Hu, Y.; Mei, A.; Han, H. Degradation pathways in perovskite solar cells and how to meet international standards. *Commun. Mater.* **2022**, *3*, 58. [[CrossRef](#)]
27. Kulbak, M.; Gupta, S.; Kedem, N.; Levine, I.; Bendikov, T.; Hodes, G.; Cahen, D. Cesium Enhances Long-Term Stability of Lead Bromide Perovskite-Based Solar Cells. *J. Phys. Chem. Lett.* **2016**, *7*, 167–172. [[CrossRef](#)]
28. Møller, C. Crystal Structure and Photoconductivity of Cesium Plumbahalides. *Nature* **1958**, *182*, 1436. [[CrossRef](#)]
29. Brinck, S.T.; Infante, I. Surface Termination, Morphology, and Bright Photoluminescence of Cesium Lead Halide Perovskite Nanocrystals. *ACS Energy Lett.* **2016**, *1*, 1266–1272. [[CrossRef](#)]
30. Rakita, Y.; Kedem, N.; Gupta, S.; Sadhanala, A.; Kalchenko, V.; Böhm, M.L.; Kulbak, M.; Friend, R.H.; Cahen, D.; Hodes, G. Low-Temperature Solution-Grown CsPbBr₃ Single Crystals and Their Characterization. *Cryst. Growth Des.* **2016**, *16*, 5717–5725. [[CrossRef](#)]
31. He, X.; Qiu, Y.; Yang, S. Fully-Inorganic Trihalide Perovskite Nanocrystals: A New Research Frontier of Optoelectronic Materials. *Adv. Mater.* **2017**, *29*, 1700775. [[CrossRef](#)] [[PubMed](#)]
32. Fang, F.; Chen, W.; Li, Y.; Liu, H.; Mei, M.; Zhang, R.; Hao, J.; Mikita, M.; Cao, W.; Pan, R.; et al. Employing Polar Solvent Controlled Ionization in Precursors for Synthesis of High-Quality Inorganic Perovskite Nanocrystals at Room Temperature. *Adv. Funct. Mater.* **2018**, *28*, 1706000. [[CrossRef](#)]
33. Tenailleau, C.; Aharon, S.; Cohen, B.-E.; Etgar, L. Cell refinement of CsPbBr₃ perovskite nanoparticles and thin films. *Nanoscale Adv.* **2019**, *1*, 147–153. [[CrossRef](#)]
34. Grisorio, R.; Fanizza, E.; Allegretta, I.; Altamura, D.; Striccoli, M.; Terzano, R.; Giannini, C.; Vergaro, V.; Ciccarella, G.; Margiotta, N.; et al. Insights into the role of the lead/surfactant ratio in the formation and passivation of cesium lead bromide perovskite nanocrystals. *Nanoscale* **2020**, *12*, 623–637. [[CrossRef](#)] [[PubMed](#)]
35. Xu, F.; Zhang, M.; Li, Z.; Yang, X.; Zhu, R. Challenges and Perspectives toward Future Wide-Bandgap Mixed-Halide Perovskite Photovoltaics. *Adv. Energy Mater.* **2023**, *13*, 2203911. [[CrossRef](#)]
36. Xu, F.; Demir, H.V. LEDs using halide perovskite nanocrystal emitters. *Nanoscale* **2019**, *11*, 11402–11412.
37. Zhao, Y.; Zhu, K. Organic–inorganic hybrid lead halide perovskites for optoelectronic and electronic applications. *Chem. Soc. Rev.* **2016**, *45*, 655–689. [[CrossRef](#)] [[PubMed](#)]
38. Zhu, X.; Ge, L.; Wang, Y.; Li, M.; Zhang, R.; Xu, M.; Zhao, Z.; Lv, W.; Chen, R. Recent Advances in Enhancing and Enriching the Optical Properties of Cl-Based CsPbX₃ Nanocrystals. *Adv. Opt. Mater.* **2021**, *9*, 2100058. [[CrossRef](#)]
39. Xiang, W.; Liu, S.F.; Tress, W. A review on the stability of inorganic metal halide perovskites: Challenges and opportunities for stable solar cells. *Energy Environ. Sci.* **2021**, *14*, 2090–2113. [[CrossRef](#)]
40. Alaei, A.; Circelli, A.; Yuan, Y.; Yang, Y.; Lee, S.S. Polymorphism in metal halide perovskites. *Mater. Adv.* **2021**, *2*, 47–63. [[CrossRef](#)]
41. Calistru, D.M.; Mihut, L.; Lefrant, S.; Baltog, I. Identification of the symmetry of phonon modes in CsPbCl₃ in phase IV by Raman and resonance-Raman scattering. *J. Appl. Phys.* **1997**, *82*, 5391–5395. [[CrossRef](#)]
42. Trots, D.M.; Myagkota, S.V. High-temperature structural evolution of caesium and rubidium triiodoplumbates. *J. Phys. Chem. Solids* **2008**, *69*, 2520–2526. [[CrossRef](#)]
43. Lai, M.; Kong, Q.; Bischak, C.G.; Yu, Y.; Dou, L.; Eaton, S.W.; Ginsberg, N.S.; Yang, P. Structural, optical, and electrical properties of phase-controlled cesium lead iodide nanowires. *Nano Res.* **2017**, *10*, 1107–1114. [[CrossRef](#)]
44. Ahmad, M.; Rehman, G.; Ali, L.; Shafiq, M.; Iqbal, R.; Ahmad, R.; Khan, T.; Jalali-Asadabadi, S.; Maqbool, M.; Ahmad, I. Structural, electronic and optical properties of CsPbX₃ (X = Cl, Br, I) for energy storage and hybrid solar cell applications. *J. Alloys Compd.* **2017**, *705*, 828–839. [[CrossRef](#)]

45. He, Y.; Stoumpos, C.C.; Hadar, I.; Luo, Z.; McCall, K.M.M.; Liu, Z.; Chung, D.Y.; Wessels, B.W.; Kanatzidis, M.G. Demonstration of Energy-Resolved γ -Ray Detection at Room Temperature by the CsPbCl₃ Perovskite Semiconductor. *J. Am. Chem. Soc.* **2021**, *143*, 2068–2077. [[CrossRef](#)]
46. Eperon, G.G.; Paterno, G.M.; Sutton, R.J.; Zampetti, A.; Haghighirad, A.A.; Cacialli, F.; Snaith, H.J. Inorganic caesium lead iodide perovskite solar cells. *J. Mater. Chem. A* **2015**, *3*, 19688–19695. [[CrossRef](#)]
47. Liao, M.; Shan, B.; Li, M. In Situ Raman Spectroscopic Studies of Thermal Stability of All-Inorganic Cesium Lead Halide (CsPbX₃, X = Cl, Br, I) Perovskite Nanocrystals. *J. Phys. Chem. Lett.* **2019**, *10*, 1217–1225. [[CrossRef](#)]
48. Boote, B.W.; Andaraarachchi, H.P.; Rosales, B.A.; Blome-Fernández, R.; Zhu, F.; Reichert, M.D.; Santra, K.; Li, J.; Petrich, J.W.; Vela, J.; et al. Unveiling the Photo- and Thermal-Stability of Cesium Lead Halide Perovskite Nanocrystals. *Chem. Phys. Chem.* **2019**, *20*, 2647–2656. [[CrossRef](#)]
49. Stoumpos, C.C.; Malliakas, C.D.; Peters, J.A.; Liu, Z.; Sebastian, M.; Im, J.; Chasapis, T.C.; Wibowo, A.C.; Chung, D.Y.; Freeman, A.J.; et al. Crystal Growth of the Perovskite Semiconductor CsPbBr₃: A New Material for High-Energy Radiation Detection. *Cryst. Growth Des.* **2013**, *13*, 2722–2727. [[CrossRef](#)]
50. Kobayashi, M.; Omata, K.; Sugimoto, S.; Tamagawa, Y.; Kuroiwa, T.; Asada, H.; Takeuchi, H.; Kondo, S. Scintillation characteristics of CsPbCl₃ single crystals. *Nucl. Instrum. Methods Phys. Res. A* **2008**, *592*, 369–373. [[CrossRef](#)]
51. Protesescu, L.; Yakunin, S.; Bodnarchuk, M.I.; Krieg, F.; Caputo, R.; Hendon, C.H.; Yang, R.X.; Walsh, A.; Kovalenko, M.V. Nanocrystals of Cesium Lead Halide Perovskites (CsPbX₃, X = Cl, Br, and I): Novel Optoelectronic Materials Showing Bright Emission with Wide Color Gamut. *Nano Lett.* **2015**, *15*, 3692–3696. [[CrossRef](#)] [[PubMed](#)]
52. Li, X.; Wu, Y.; Zhang, S.; Cai, B.; Gu, Y.; Song, J.; Zeng, H. CsPbX₃ Quantum Dots for Lighting and Displays: Room-Temperature Synthesis, Photoluminescence Superiorities, Underlying Origins and White Light-Emitting Diodes. *Adv. Funct. Mater.* **2016**, *26*, 2435–2445. [[CrossRef](#)]
53. Xu, H.; Wang, J.; Xuan, T.; Lv, C.; Hou, J.; Zhang, L.; Dong, Y.; Shi, J. Convenient and large-scale synthesis of high-quality, all-inorganic lead halide perovskite nanocrystals for white light-emitting diodes. *Chem. Eng. J.* **2019**, *364*, 20–27. [[CrossRef](#)]
54. Zhang, Y.; Li, G.; She, C.; Liu, S.; Yue, F.; Jing, C.; Cheng, Y.; Chu, J. Room temperature preparation of highly stable cesium lead halide perovskite nanocrystals by ligand modification for white light-emitting diodes. *Nano Res.* **2021**, *14*, 2770–2775. [[CrossRef](#)]
55. Ghorai, A.; Mahato, S.; Srivastava, S.K.; Ray, S.K. Atomic Insights of Stable, Monodispersed CsPbI₃-xBr_x (x = 0, 1, 2, 3) Nanocrystals Synthesized by Modified Ligand Cell. *Adv. Funct. Mater.* **2022**, *32*, 2202087. [[CrossRef](#)]
56. La Mer, V.K. Nucleation in Phase Transitions. *Ind. Eng. Chem.* **1952**, *44*, 1270–1277. [[CrossRef](#)]
57. Jung, M.; Ji, S.-G.; Kim, G.; Seok, S.-I. Perovskite precursor solution chemistry: From fundamentals to photovoltaic applications. *Chem. Soc. Rev.* **2019**, *48*, 2011–2038. [[CrossRef](#)] [[PubMed](#)]
58. Jeon, N.J.; Noh, J.H.; Kim, Y.C.; Yang, W.S.; Ryu, S.; Seok, S.I. Solvent engineering for high-performance inorganic–organic hybrid perovskite solar cells. *Nat. Mater.* **2014**, *13*, 897–903. [[CrossRef](#)]
59. Xiao, M.A.; Huang, F.; Huang, W.; Dkhissi, Y.; Zhu, Y.; Etheridge, J.; Gray-Weale, A.; Bach, U.; Cheng, Y.-B.; Spiccia, L. Fast Deposition–Crystallization Procedure for Highly Efficient Lead Iodide Perovskite Thin-Film Solar Cells. *Angew. Chem. Int. Ed.* **2014**, *53*, 9898–9903. [[CrossRef](#)]
60. Rodová, M.; Brožek, J.; Knížek, K.; Nitsch, K. Phase transitions in ternary caesium lead bromide. *J. Therm. Anal. Calorim.* **2003**, *71*, 667–673. [[CrossRef](#)]
61. Malyshkin, D.; Sereda, V.; Ivanov, I.; Mazurin, M.; Sednev-Lugovets, A.; Tsvetkov, D.; Zuev, A. New phase transition in CsPbBr₃. *Mater. Lett.* **2020**, *278*, 128458. [[CrossRef](#)]
62. Nikou, T.; Witt, M.; Stathopoulos, P.; Barsch, A.; Halabalaki, M. Olive Oil Quality and Authenticity Assessment Aspects Employing FIA-MRMS and LC-Orbitrap MS Metabolomic Approaches. *Front. Public Health* **2020**, *8*, 558226. [[CrossRef](#)] [[PubMed](#)]
63. Noh, J.H.; Im, S.H.; Heo, J.H.; Mandal, T.N.; Seok, S.I. Chemical Management for Colorful, Efficient, and Stable Inorganic–Organic Hybrid Nanostructured Solar Cells. *Nano Lett.* **2013**, *13*, 1764–1769. [[CrossRef](#)]
64. Jeon, N.J.; Noh, J.H.; Yang, W.S.; Kim, Y.C.; Ryu, S.; Seo, J.; Seok, S.I. Compositional engineering of perovskite materials for high-performance solar cells. *Nature* **2015**, *517*, 476–480. [[CrossRef](#)] [[PubMed](#)]
65. Jang, Y.-W.; Lee, S.; Yeom, K.M.; Jeong, K.; Choi, K.; Choi, M.; Noh, J.H. Intact 2D/3D halide junction perovskite solar cells via solid-phase in-plane growth. *Nat. Energy* **2021**, *6*, 63–71. [[CrossRef](#)]
66. Zhou, Y.-Q.; Xu, J.; Liu, J.-B.; Liu, B.-X. Alloy engineering in mixed Sn–Ge perovskites for photovoltaic application. *J. Mater. Chem. A* **2021**, *9*, 6955–6961. [[CrossRef](#)]
67. Li, J.; Yan, N.; Fang, Z.; Liu, S.F. Alkyl Diamine-Induced (100)-Preferred Crystal Orientation for Efficient Pb–Sn Perovskite Solar Cells. *ACS Appl. Energy Mater.* **2022**, *5*, 6936–6942. [[CrossRef](#)]
68. Gutmann, V. Solvent effects on the reactivities of organometallic compounds. *Coord. Chem. Rev.* **1976**, *18*, 225–255. [[CrossRef](#)]
69. Belmares, M.; Blanco, M.; Goddard, W.A., III; Ross, R.B.; Caldwell, G.; Chou, S.-H.; Pham, J.; Olofson, P.M.; Thomas, C. Hildebrand and Hansen solubility parameters from molecular dynamics with applications to electronic nose polymer sensors. *J. Comput. Chem.* **2004**, *25*, 1814–1826. [[CrossRef](#)]
70. Yan, K.; Long, M.; Zhang, T.; Wei, Z.; Chen, H.; Yang, S.; Xu, J. Hybrid Halide Perovskite Solar Cell Precursors: Colloidal Chemistry and Coordination Engineering behind Device Processing for High Efficiency. *J. Am. Chem. Soc.* **2015**, *137*, 4460–4468. [[CrossRef](#)]

71. Petrov, A.A.; Ordinartsev, A.A.; Fateev, S.A.; Goodilin, E.A.; Tarasov, A.B. Solubility of Hybrid Halide Perovskites in DMF and DMSO. *Molecules* **2021**, *26*, 7541. [[CrossRef](#)]
72. Huangfu, C.; Feng, L. High-performance fluorescent sensor based on CsPbBr₃ quantum dots for rapid analysis of total polar materials in edible oils. *Sens. Actuators B Chem.* **2021**, *344*, 130193. [[CrossRef](#)]
73. Chen, H.; Wang, Y.; Wang, J.; Liu, W. Thermal Stability of CsPbBr₃ Perovskite Quantum Dots Assembled with SBA-15. *Coatings* **2021**, *11*, 953. [[CrossRef](#)]
74. Mott, S.N. The mobility edge since 1967. *J. Phys. C Solid State Phys.* **1987**, *20*, 3075–3102. [[CrossRef](#)]
75. Smith, B.C. *Infrared Spectral Interpretation: A Systematic Approach*; CRC Press: Boca Raton, FL, USA, 1999.
76. Akhil, S.; Dutt, V.G.V.; Mishra, N. Surface modification for improving the photoredox activity of CsPbBr₃ nanocrystals. *Nanoscale Adv.* **2021**, *3*, 2547–2553. [[CrossRef](#)] [[PubMed](#)]

Disclaimer/Publisher's Note: The statements, opinions and data contained in all publications are solely those of the individual author(s) and contributor(s) and not of MDPI and/or the editor(s). MDPI and/or the editor(s) disclaim responsibility for any injury to people or property resulting from any ideas, methods, instructions or products referred to in the content.